,

Enhanced extreme ultraviolet high-harmonic generation from chromium-doped magnesium oxide

V. E. Nefedova,[1] S. Fröhlich,[1] F. Navarrete,[2,3] N. Tancogne-Dejean,[4] D. Franz,[1] A. Hamdou,[1] S. Kaassamani,[1] D. Gauthier,[1] R. Nicolas,[1,5] G. Jargot,[6,7] M. Hanna,[6] P. Georges,[6] M. F. Ciappina,[8,9,10] U. Thumm,[2,a)] W. Boutu,[1] and H. Merdji[1,b)]

[1)] *Ultrafast Nanophotonics group, LIDYL, CEA-CNRS-Université Paris-Saclay 91191, Gif-sur-Yvette, France*

[2)] *Department of Physics, Kansas State University, Manhattan, KS 66506, USA*

[3)] *Institute of Physics, University of Rostock, 18051 Rostock, Germany*

[4)] *Max Planck Institute for the Structure and Dynamics of Matter and Center for Free-Electron Laser Science, Luruper Chaussee 149, 22761 Hamburg, Germany*

[5)] *Department of Natural Sciences, Lebanese American University, 1102 Beirut, Lebanon*

[6)] *Université Paris-Saclay, Institut d'Optique Graduate School, CNRS, Laboratoire Charles Fabry, 91127, Palaiseau, France*

[7)] *Fastlite, 06600 Antibes, Sophia Antipolis, France*

[8)] *ICFO-Institut de Ciences Fotoniques, The Barcelona Institute of Science and Technology, Avenue Carl Friedrich Gauss 3, 08860 Castelldefels (Barcelona), Spain*

[9)] *Physics Program, Guangdong Technion – Israel Institute of Technology, Shantou, Guangdong 515063, China*

[10)] *Technion – Israel Institute of Technology, Haifa, 32000, Israel*

(Dated: 12 April 2021)

SI.1. PHOTOLUMINESCENCE MEASUREMENTS ON MgO AND MgO:Cr

In order to confirm the presence of Cr^{3+} ions in the MgO:Cr crystal, we perform photoluminescence (PL) measurements on both, MgO and MgO:Cr samples, and compare the obtained signals. The PL measurements are done at room temperature with an excitation wavelength of 365 nm. The source signal is filtered out before the detection, using a long-pass filter with a cutoff wavelength of 514 nm. The PL signal is detected by a spectrometer (Ocean Optics QE Pro Spectrometer).

Figure S1 shows the PL signals from both samples. There is a strong PL signal from MgO:Cr, which consists of multiple peaks with a broad feature around 700 - 800 nm. Such a behavior of the PL signal is typically attributed to $^4T_2 \rightarrow {}^4A_2$ transitions from Cr^{3+} ions in orthorhombic sites in MgO[1–3]. Therefore, our PL measurements experimentally confirm the presence of Cr^{3+} ions in the MgO:Cr sample, which lead to the formation of Mg vacancies. Photoluminescence measurements in MgO reveal peaks near 720 nm as well as around 850-950 nm. We attribute these features to impurities in the undoped MgO sample, the signal around 720 nm being probably associated with Cr impurities, while multiple lines around 850-950 nm may be due to $Mg(OH)_2$ contamination. A similar PL behavior from MgO undoped samples was reported in previous works[4–8].

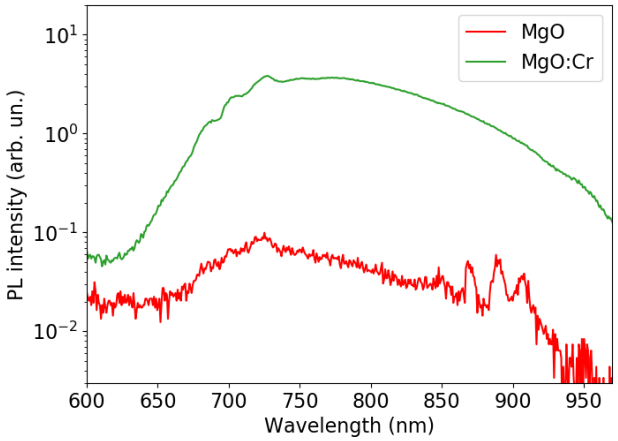

FIG. S1: Measured photoluminescence signal from the MgO and MgO:Cr samples excited at a wavelength of 365 nm at room temperature. Both curves are on the same scale.

SI.2. OPTICAL CHARACTERIZATION AND PROPERTIES OF PRISTINE AND CHROMIUM-DOPED MgO

In order to obtain information about the band-gap energies of our MgO and MgO:Cr samples with 5000 ppm chromium concentration (corresponding to $\sim 0.5\%$ defect concentration), we measure the transmission of white light through the samples. We apply the Tauc method of optical absorption-edge determination[9]. This method is used to determine the optical band gap in semiconductors. The obtained Tauc plots are shown in Fig. S2. The linear region of the curve has to

a)Corresponding author, email address: thumm@phys.ksu.edu

b)Corresponding author, email address: hamed.merdji@cea.fr

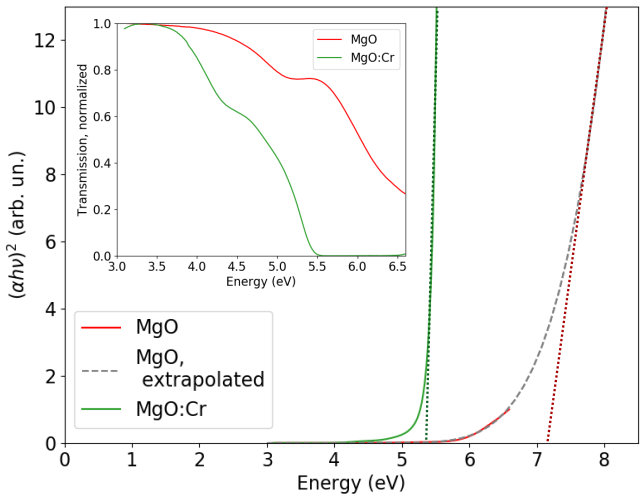

FIG. S2: Tauc plots (and transmission curves as an insert) of the MgO and MgO:Cr samples, where $h\nu$ is the photon energy and α the absorption coefficient (calculated from the measured transmission data).

be extrapolated for the determination of the band-gap energy. We infer from the data a band-gap energy for MgO:Cr of about 5.36 eV. The energy range of the detector is limited to a maximum photon energy of 6.52 eV. For energies above 6.52 eV, we use a fifth-order polynomial extrapolation in the Tauc plot. The linear region in the extrapolated Tauc plot for MgO provides a band-gap energy of 7.16 eV. The band-gap-energy difference between the doped and undoped crystals is around 1.8 eV. We note that the commonly used value for the band-gap energy of the pristine MgO is 7.8 eV[10]. The observed modification of the band structure, with the consequent band-gap narrowing in MgO:Cr compared to MgO, results from vacancies imposed by added Cr^{3+} ions in MgO that preserve charge neutrality[11,12].

In alkali halides, the exciton transitions near the cation vacancy are known to be responsible for the band-gap change[13,14]. The possible presence of vacancy-induced exciton is difficult to determine precisely from our transmission data. The observed band-gap narrowing could be a combined effect of both: the presence of in-gap states and a vacancy-induced exciton. From the one hand, our DFT calculations provided in SI.4 confirm the effect of the bandgap reduction due to defect states in the bandgap. From another hand, the importance of the binding energy of the exciton for our samples is not yet determined. The possible role of excitonic effects on the band-gap modification of our samples is a subject for future investigations.

The optical properties of MgO crystal are given in Table S1 for the driving laser wavelength $\lambda = 1550$ nm as well as for two high harmonic orders in the HHG plateau spectral region, harmonic order 21 ($\lambda = 73.81$ nm; E = 16.79 eV) and 23 ($\lambda = 67.39$ nm; E = 18.39 eV). The complex refractive index n^* is given by $n^* = n_r + in_i$. The attenuation length (defined as the distance over which the intensity of the radiation drops to $1/e$ compared to the initial value) is given by[15]

	IR laser	HH_{21}	HH_{23}
λ (nm)	1550	73.81	67.39
n^*	$1.71+1\times10^{-6}i$	$1.31+0.98i$	$0.89+0.99i$
l_{at} (nm)	123×10^{6}	6.00	5.42

TABLE S1: Complex refractive index n^* and attenuation length l_{at} for MgO for the driving laser and harmonic orders 21 and 23.

$l_{at} = \lambda/4\pi n_i$. According to the calculated data provided in Table S1, the attenuation length for XUV high-order harmonics in the MgO crystal is only few nanometers. Therefore, the detected high-order-harmonic radiation is produced from a very narrow layer at the rear side of the crystal.

While the n_i values in the XUV region are well established[16,17], the data at 1550 nm vary from few times 10^{-6} to 2×10^{-8} with the quality of the crystals[17] (and references therein). Taking the upper limit of n_i as 1×10^{-6} results in an attenuation length of l_{at}=12.3 mm. According to the Beer-Lambert law, the transmission of light through our crystal is $T = \exp(-\alpha z)$, where $\alpha = 1/l_{at}$ is the absorption coefficient, and z the thickness of the material. This implies a transmission of 98% of the driving-pulse intensity for a 200 μm thick MgO sample.

It is important to compare the values of the optical properties of MgO and MgO:Cr. However, to the best of our knowledge, the optical constants for MgO:Cr with 5000 ppm dopant concentration are not tabulated. According to the literature on wide bandgap crystals (as Ti:Sapphire, CaF_2 or SrF_2) with low dopant concentrations[18–21], we assume that for our conditions the refractive index of the pristine crystal can be used for the doped one and, therefore, that propagation effects are similar in both crystals, without affecting our analysis. Possible effects of nonlinear phenomena, such as Kerr self focusing, are currently under investigation.

SI.3. THEORETICAL MODEL FOR HHG IN SOLIDS WITH VACANCY DEFECTS

We numerically solve the Semiconductor Bloch Equations (SBEs)[22–28]

$$\left[\hat{H}, \hat{\rho}(t)\right] = i\dot{\hat{\rho}}(t)\,, \tag{S1}$$

where $\hat{\rho}(t)$ is the density operator. The Hamiltonian of the system can be written in the velocity gauge as

$$\begin{aligned}\hat{H} &= \frac{1}{2}\hat{\mathbf{p}}^2 + \mathbf{A}(t)\cdot\hat{\mathbf{p}} + V(\mathbf{r}) \\ &= \hat{H}_0 + \mathbf{A}(t)\cdot\hat{\mathbf{p}}\,,\end{aligned} \tag{S2}$$

where $\hat{\mathbf{p}}$ is the momentum operator, $\mathbf{A}(t)$ the vector potential of the driving laser pulse, and $V(\mathbf{r})$ the lattice potential. We

approximate the lattice potential in separated Cartesian coordinates,

$$V(\mathbf{r}) = V(x) + V(y) \,. \tag{S3}$$

Throughout this supplement we use atomic units, unless indicated otherwise. The field-free Hamiltonian and its eigenstates are given by

$$\hat{H}_0 \left|\phi_{n\mathbf{k}}\right\rangle = \varepsilon_{n\mathbf{k}} \left|\phi_{n\mathbf{k}}\right\rangle \,. \tag{S4}$$

The corresponding field-free energy eigenvalues are $\varepsilon_{n\mathbf{k}}$. n is the band index and $\mathbf{k}$ the crystal momentum. For the potential (S3) the eigenstates separate into 1D states along the x and y coordinate,

$$\left|\phi_{n\mathbf{k}}\right\rangle = \left|\phi_{nk_x}\right\rangle \left|\phi_{nk_y}\right\rangle \,, \tag{S5}$$

where

$$\hat{H}_{0j} \left|\phi_{nk_j}\right\rangle = \varepsilon_{nk_j} \left|\phi_{nk_j}\right\rangle \,, \quad j = x, y \,. \tag{S6}$$

The projection operator $\hat{\rho}_{\mathbf{k}}(t)$ for any crystal momentum $\mathbf{k}$ in the first Brillouin zone(BZ) can be written as

$$\hat{\rho}_{\mathbf{k}}(t) = \left|\psi_{\mathbf{k}}(t)\right\rangle \left\langle\psi_{\mathbf{k}}(t)\right| \,, \tag{S7}$$

in terms of solutions $\left|\psi_{\mathbf{k}}(t)\right\rangle$ of the time-dependent Schrödinger equation (TDSE)

$$\hat{H} \left|\psi_{\mathbf{k}}(t)\right\rangle = i\frac{d}{dt} \left|\psi_{\mathbf{k}}(t)\right\rangle \,. \tag{S8}$$

Assuming a spatially homogeneous driving laser field, we separate the Hamiltonian (S2),

$$\hat{H} = \hat{H}_x^{int} + \hat{H}_y^{int} \,, \tag{S9}$$

where

$$\hat{H}_j^{int} = \hat{H}_{0j} + A_{0j}(t) r_j \,, \quad j = x, y \,, \tag{S10}$$

with $r_x = x$ and $r_y = y$. Separating the projection in Cartesian coordinates,

$$\begin{aligned} \hat{\rho}_{\mathbf{k}}(t) &= \hat{\rho}_{k_x}(t) \hat{\rho}_{k_y}(t) \\ &= \left|\psi_{k_x}(t)\right\rangle \left\langle\psi_{k_x}(t)\right| \left|\psi_{k_y}(t)\right\rangle \left\langle\psi_{k_y}(t)\right| \,, \end{aligned} \tag{S11}$$

and expanding in eigenstates of $\hat{H}_{0j}$,

$$\left|\psi_{k_j}(t)\right\rangle = \sum_n B_{nk_j}(t) \left|\phi_{nk_j}\right\rangle \,, \tag{S12}$$

we obtain from the Liouville equation

$$\left[\hat{H}_x^{int} + \hat{H}_y^{int}, \hat{\rho}(t)\right] = i\dot{\hat{\rho}}(t) \tag{S13}$$

the SBEs

$$\begin{aligned} i\dot{\rho}_{k_j}^{nn'}(t) = &-i\frac{\rho_{k_j}^{nn'}(t)}{T_2} + \left(\varepsilon_{nk_j} - \varepsilon_{n'k_j}\right) \rho_{k_j}^{nn'}(t) \\ &+ A_j(t) \sum_{n''} [P_{k_j}^{nn''} \rho_{k_j}^{n''n'}(t) - P_{k_j}^{n''n'} \rho_k^{nn''}(t)] \end{aligned} \tag{S14}$$

for the time evolution of the density operator in eigenstate matrix representation,

$$\begin{aligned} \rho_{k_j}^{nn'}(t) &= B_{nk_j}(t) B_{n'k_j}^*(t) \\ &= \left\langle \phi_{nk_j} \right| \hat{\rho}_{k_j} \left| \phi_{n'k_j} \right\rangle \,. \end{aligned}$$

The diagonal elements $\rho_{k_j}^{nn'}(t)$ represent populations of bands n, and the momentum matrix elements are defined as

$$P_{k_j}^{nn'} = \left\langle \phi_{nk_j} \right| \hat{p}_j \left| \phi_{n'k_j} \right\rangle \,. \tag{S15}$$

T_2 is a phenomenological dephasing time, introduced to account for polarization damping[29], which can also be derived formally by extending the formalism to include many-body interactions, coupling with phonons, and electron-electron scattering[29].

The laser-driven electronic current for an initial crystal momentum $\mathbf{k}$ is

$$\mathbf{J}_{\mathbf{k}}(t) = J_{k_x}(t)\hat{\mathbf{x}} + J_{k_y}(t)\hat{\mathbf{y}} \,, \tag{S16}$$

with Cartesian components

$$J_{k_j}(t) = -\sum_{n'} \sum_{n} \left\langle \phi_{nk_j} \right| \hat{\rho}_{k_j} \left| \phi_{n'k_j} \right\rangle \left\langle \phi_{nk_j} \right| \hat{p}_j \left| \phi_{n'k_j} \right\rangle - A_j(t) \,. \tag{S17}$$

The total current and its components follow as

$$\begin{aligned} \mathbf{J}(t) &= \int_{BZ} J_{\mathbf{k}}(t) d^2\mathbf{k} \\ &= \frac{2\pi}{a}\hat{\mathbf{x}} \int_{-\pi/a}^{\pi/a} J_{k_x}(t) dk_x + \frac{2\pi}{a}\hat{\mathbf{y}} \int_{-\pi/a}^{\pi/a} J_{k_y}(t) dk_y \\ &= J_x(t)\hat{\mathbf{x}} + J_y(t)\hat{\mathbf{y}} \,, \end{aligned} \tag{S18}$$

allowing us to calculate the spectral HHG yield as

$$\begin{aligned} Y(\omega) &= \left| \int_{-\infty}^{\infty} dt\, e^{-i\omega t} \mathbf{J}(t) \right|^2 \equiv \left| \hat{\mathbf{J}}(\omega) \right|^2 \\ &= \left| \int_{-\infty}^{\infty} dt\, e^{-i\omega t} \left[J_x(t)\hat{\mathbf{x}} + J_y(t)\hat{\mathbf{y}} \right] \right|^2 \\ &\equiv \left| \hat{J}_x(\omega) \right|^2 + \left| \hat{J}_y(\omega) \right|^2 . \end{aligned} \tag{S19}$$

We model the MgO band structure in each spatial dimension by the cosine potential[25,30,31]

$$V_j(x) = V_0 \cos(a r_j) \,, \tag{S20}$$

with V_0 =0.37 a.u. and lattice parameter $a = 8$ a.u. Even though this potential matches adequately the bandwidth of the two lowest bands of MgO in the $\Gamma - X$ direction, it produces a minimum band gap of 4.2 eV. We therefore shift the valence band downwards[32] to adjust the minimum band gap to the experimental value of 7.8 eV (Fig. S3).

We represent the MgO:Cr band structure for 0.5% Cr doping taking into account both, the substitution of Mg by Cr ions and the presence of Mg vacancies, by modifying the potential of the pristine sample[33–37]. To account for the effect of

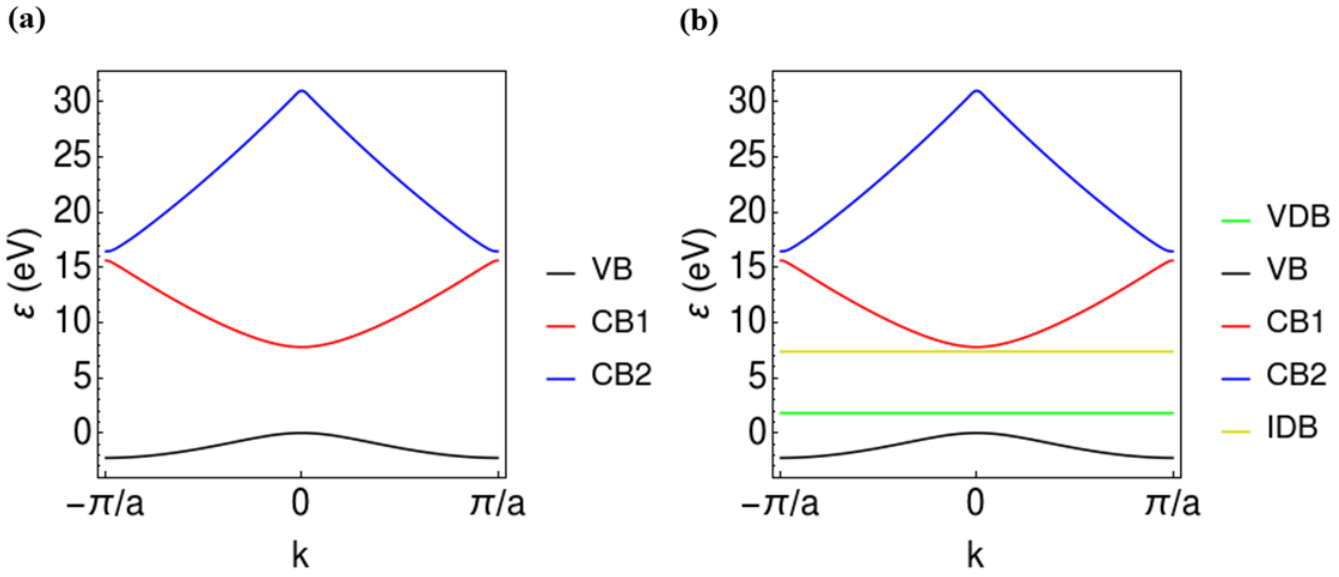

FIG. S3: Energy bands used in the calculation. Valence (VB) and two conduction bands (CB1 and CB2) of the (a) pristine MgO and (b) MgO:Cr crystal. Panel (b) includes the vacancy defect (VDB) and impurity defect (IDB) bands of MgO:Cr.

vacancies, we increase the oscillation amplitude at a position $n_{vac}a$. Furthermore, accounting for the substitution of Mg^{2+} by Cr^{3+}, we decrease the oscillation amplitude at a neighbouring lattice position $n_{imp}a$. This results in the modified electronic potential

$$V_j(x) = V_0\cos(ar_j) + \begin{cases} V_{vac}\cos(ar_j)\,, \\ \quad n_{vac}a \le x \le (n_{vac}+1)a \\ V_{imp}\cos(ar_j)\,, \\ \quad n_{imp}a \le x \le (n_{imp}+1)a \end{cases}, \quad \text{(S21)}$$

where V_0, V_{vac}, and V_{imp} are the pristine solid, the impurity, and the vacancy potential strength, respectively. The 0.5% dopant concentration amounts to one Cr ion for every 200 lattice sites. We match the band gap reduction of 1.8 eV observed for MgO:Cr (Sec. SI.2) for V_{imp}=0.11 a.u. and V_{vac}= -0.11 a.u. For the low dopant concentrations used in the present work, we may approximate defect states as non-dispersive levels in the band gap with an infinite effective mass. These states couple along the entire BZ to excite conduction band levels[37]. This coupling is allowed since the presence of impurities breaks the translational symmetry of the pristine lattice, while the pristine MgO crystal only allows optical transitions between states of equal crystal momentum within the first BZ. However, due to our low defect concentration, the electronic band structure of MgO is only slightly modified, consistent with our DFT calculations (Sec. SI.4). We therefore approximate the coupling between bands as strictly vertical. In summary, we model the band structure of MgO:Cr used in our calculation in terms of dispersive valence- and conduction-bands of the pristine crystal with two modifications: (i) an adjusted band-gap energy (Sec. SI.2.) and two added flat (i.e., non-dispersive) bands accounting for vacancy and impurity states, as shown in Fig. S3.

Neglecting temperature effects, the Fermi level for the doped crystal lies between the valence and lowest conduction band of MgO[38]. The valence band and vacancy state are thus occupied, while higher bands are unoccupied.

The weak yield of HH 18 from MgO:Cr is likely due to numerical noise brought into our SBE solution by the added IDB and VDB (Fig. 2). Numerically, noise can be reduced by assuming a very small dephasing time. Even though a precise experimental quantification of the dephasing time is difficult, taking extremely small dephasing has been described as unphysical[28]. We here decided to employ a constant dephasing time T_2, adjusted to a quarter-cycle of driving-laser optical period, following Ref.[25]. When integrating the yield, we only include odd harmonics, in order to not over-estimate the yield from the doped sample, because, as shown Fig. 2 (b), the numerical calculation for the doped sample exhibits low-contrast spurious even harmonic contributions at high intensities, which are not observed experimentally.

We model the laser field with a 5-cycle flat-top envelope. In all calculations we employ a fourth-order Runge-Kutta algorithm to numerically solve the SBE (S14) at 400 equally spaced $k-$points in the first BZ.

SI.4. APPEARANCE OF VACANCY-INDUCED DEFECT STATES IN MgO:Cr FROM DENSITY FUNCTIONAL THEORY

We perform *ab initio* density functional theory (DFT) simulations of the doped MgO with $6\times6\times6$ supercells, using only the Γ point to represent the Brillouin zone. This yields a defect

concentration of 0.46%, very similar to the 5000 ppm concentration of the experimental samples. To get a reliable band-gap energy, we employ the Tran-Blaha (TB09) functional[39]. Our simulations are performed with the Octopus code[40]. We employ a grid spacing of 0.2 Bohr, norm-conserving pseudopotentials, and a lattice constant of 4.212Å. A Fermi-Dirac smearing of the electronic temperatures of 25 meV is used in all the calculations. For undoped MgO, this gives a band gap of 7.70 eV, which is quite close to the experimental value of 7.8 eV[10]. The Cr defect, as well as Mg vacancies, are non-magnetic defects. Spin degrees of freedom, as well as spin-orbit coupling, are neglected in the simulations. We investigate different situations: (i) undoped MgO, (ii) Cr-doped MgO with a concentration of 0.46% defect, (iii) Cr-doped MgO with the same concentration with a neighboring Mg vacancy. The structures have been relaxed using the Quantum Espresso code[41] at the level of the local density approximation. Various models have been proposed in the past concerning the structure of the Mg vacancy of Cr-doped MgO[42]. Here we perform simulations for both the C_{2v} and the C_{4v} structures[42], which correspond, respectively, to a vacancy located at the closest neighbor along the [110] or [100] direction.

Our results are presented in Fig. S4. Compared to undoped MgO, we find that Cr doping can introduce in-gap defect states, in agreement with previous work performed at the level of the local density approximation complemented within a Hubbard model and by experimental results[43]. We find that the Cr doping alone does not alter the valence bands of MgO, and does not produces a clear in-gap defect state, except for a defect state close to the bottom of the conduction bands. However, if we also create a Mg vacancy close to the Cr atom, we observe a significant reduction of the band gap, of about 0.6 eV, due to the appearance of defect states above the topmost valence band. We find that this complex defect center, besides adding occupied defect states within the band gap of pristine MgO, also modifies the top-most valence bands of MgO. The density of states in both cases are found to be quite similar for the C_{2v} and C_{4v} structures, indicating that the change in band gap does not rely strongly on the vacancy to be at a given neighboring site close to the Cr atom. This suggests that a simplified modeling of the defect, taking into account in-gap defect states and neglecting the microscopic details of the defect, is physically acceptable.
We performed DFT calculations for a wide range of concentrations and do not find a significant dependence of the gap on the concentration. However, the defect concentration can vary locally in the experiment.

The performed DFT calculations therefore support the results obtained by the one-dimensional model presented in Sec. SI.3. In particular, they show the position of the occupied defect state close to the top of the valence band within the gap of pristine MgO.

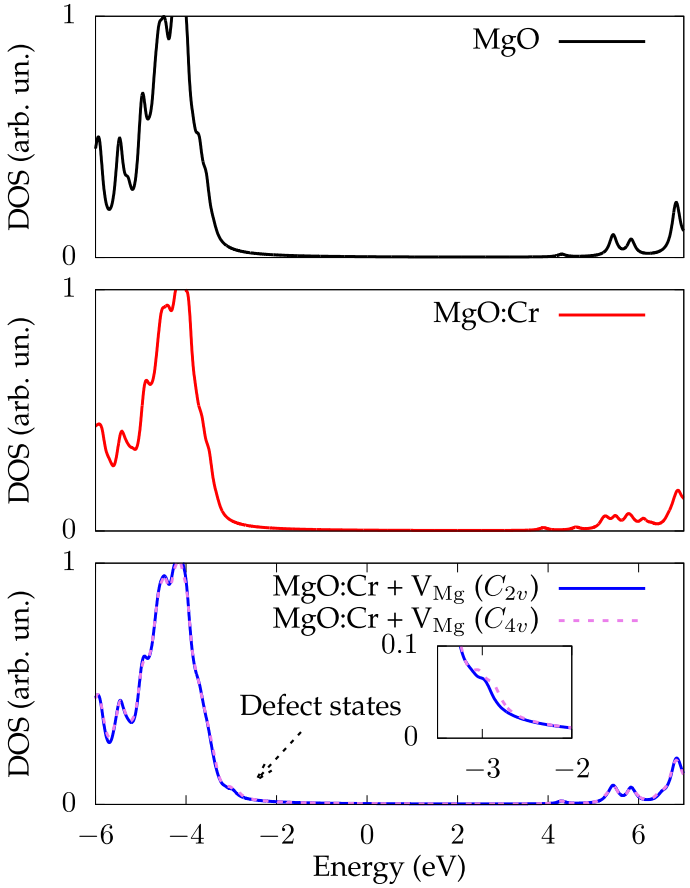

FIG. S4: Comparison of the density of states for bulk MgO (top panel), Cr-doped MgO with 5000 ppm concentration (middle panel), and Cr-doped MgO with Mg vacancies, using the C_{2v} and C_{4v} structures, as explained in the text (bottom panel).

SI.5. EXPERIMENTAL SETUP AND COMPARISON OF THE OBTAINED HHG SPECTRA

In this work, we generate harmonics in the XUV range using an intense infra-red (IR) driving field. The experiment, sketched in Fig. S5, is carried out in vacuum, at normal incidence, using a linearly-polarised laser with a wavelength centered at $\lambda_{IR} = 1.55\,\mu$m (corresponding to a photon energy of 0.80 eV), a 125 kHz repetition rate, a pulse energy on the target of up to 4 μJ, and a pulse duration of 22 fs full width at half maximum (FWHM). More details on the laser system are provided in Sec. SI.6. The laser beam is focused by a 5 cm focal length lens. The intensity at focus is estimated based on focal length, laser-pulse duration, calculated beam size in vacuum, and energy. The laser-intensity values provided are vacuum intensities. The maximum intensity estimated is I=22.5 TW/cm^2. The laser intensity is varied by rotating the half-wave plate, and the harmonic signal is optimized by moving the samples on a motorized translation stage along the optical axis. The crystal-orientation dependence of the HHG signal is investigated by rotating the crystal on a mo-

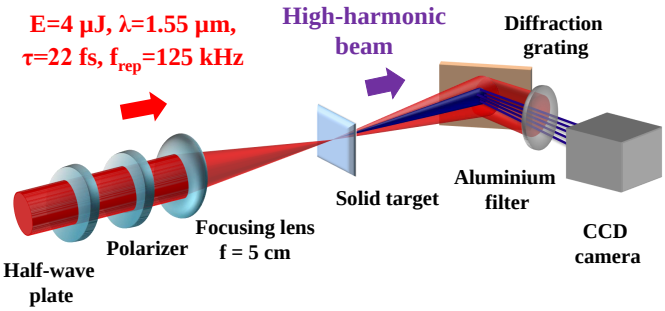

FIG. S5: (color online) Scheme of the experimental setup for HHG from MgO and MgO:Cr samples. The driving IR beam is focused into a sample producing high-order harmonics. The emitted radiation is recorded using an XUV spectrometer, which consists of a diffraction grating and a CCD camera.

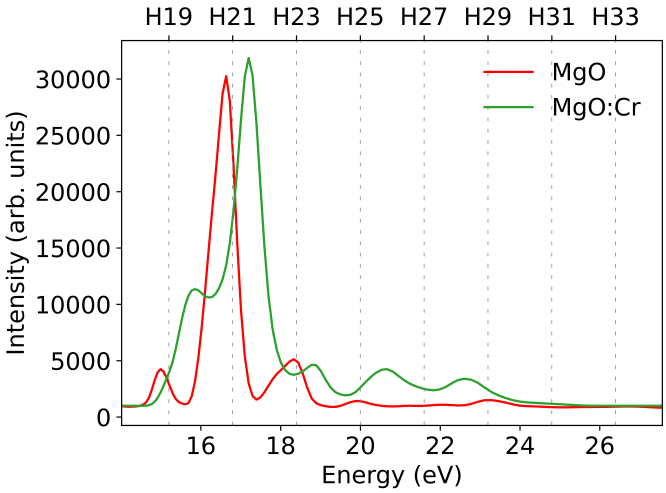

FIG. S6: Experimental HHG spectra obtained from MgO and MgO:Cr at a laser field strength of 1.05 V/Å (14.6 TW/cm^2). At fixed laser electric field the HHG spectra from MgO:Cr are more intense and blueshifted compared to MgO. The spectral shift is caused by the increased electron density involved in the HHG process in MgO:Cr

torized rotation stage around the laser-propagation axis.

The investigated samples, MgO and Cr-doped MgO, are 200-μm-thick with (001) oriented surfaces. For MgO:Cr, the doping concentration of Cr atoms is 5000 ppm (corresponding to $\sim 0.5\%$ defect concentration). The MgO:Cr sample was produced by the commercial company "SurfaceNet". Chromium atoms were introduced in MgO crystal during tri-arc plasma growth[44,45].
The interaction of the intense laser pulse with the samples results in the emission of coherent high-order harmonics, which co-propagate with the driving laser. The fundamental beam and low-order harmonics are removed by an aluminium filter allowing only XUV light to pass through it. The high-order harmonics are spectrally resolved by a home-made spectrometer composed of a reflective concave diffraction grating (McPherson 234/302, 2400 grooves/mm, Pt coated) and a back-illuminated CCD camera (Princeton Instruments, PI-MTE System; the detection exposure time was 30 seconds). The range of detected harmonics spans from order 19 (15.2 eV) to 31 (24.8 eV).

Figure S6 shows the comparison of measured HHG spectra from MgO and MgO:Cr at the laser intensity I=14.6 TW/cm^2. As can be seen, there is a HHG signal enchancement as well as spectral blueshift in case of MgO:Cr compared to MgO. We associate this wavelength shift to the increased electron density participating in HHG in MgO:Cr. In the spatial domain, the electron density is higher at the center of Gaussian beam and it decreases towards the beam edges. Due to the fact that the plasma refractive index is smaller on the beam axis, its variation acts as a diverging lens. We therefore couple the observed blueshift with plasma-induced defocusing of the fundamental beam[46–48] (and references therein).

SI.6. OPCPA LASER SYSTEM

The ultrashort pulse source at 1.55 μm relies on an optical parametric chirped pulse amplifier (OPCPA) pumped by a femtosecond ytterbium-doped fiber-based laser source at 1.03 μm. This pump source delivers 400 fs, 400 μJ pulses at 125 kHz. The OPCPA is seeded by a supercontinuum generation obtained from a small fraction of the pump laser in a YAG crystal. This signal is then temporally stretched in 5 mm of silicon, and amplified in two parametric stages. The first amplification stage is based on a MgO doped periodically poled lithium niobate (MgO:PPLN) crystal and the second one on a Potassium Titanyle Arsenate (KTiOAsO4, or KTA) crystal in non-collinear type II phase matching configuration. Compression is achieved by propagation through 210 mm of fused silica. The OPCPA output pulses are 63 fs long with an energy of 19 μJ. The pulses are then temporally compressed using soliton compression in a plate of fused silica inside a multi-pass cell. This results in the generation of 22 fs 14 μJ pulses at the cell output that are directed towards the HHG setup. The overall OPCPA architecture is described in detail in Ref.[49].

SI.7. LASER INTENSITY ESTIMATION AND NOTATION

In order to compare our experimental results with the numerical simulations, we need to be able to relate the corresponding field strengths. The intensity at the focus is estimated based on focal length, laser pulse duration, calculated beam size in vacuum, and energy. The experimental intensities are given in vacuum and do not take into account the

reflection loss on the crystal surface. Our numerical modeling relies on field strengths inside the crystals. We use the appearance of the harmonic 29 in pristine MgO as a reference for the in-vacuum field-strength value (1.23 V/Å). In this way, all field strengths used in our numerical simulations and given in the main text were corrected to in-vacuum values by multiplication with the factor 4.2.

[1] M. O. Henry, J. P. Larkin, and G. F. Imbusch, "Nature of the broadband luminescence center in MgO:Cr^{3+}," Phys. Rev. B **13**, 1893 (1976).

[2] A. Boyrivent, E. Duval, and R. Louat, "Broad band luminescence in MgO:Cr^{3+}," Solid State Communications **19**, 1221 (1976).

[3] B. Henderson and G. F. Imbusch, "Optical spectroscopy of inorganic solids," Oxford University Press **23**, 2824 (1989).

[4] C.-C.Chao, "Charge-transfer luminescence of Cr^{3+} in magnesium oxide," Journal of Physics and Chemistry of Solids **32**, 2517 (1971).

[5] Y. Kawaguchi, "Luminescence spectra at bending fracture of single crystal MgO," Solid State Communications **117**, 17 (2001).

[6] T. Kato, G. Okada, and T. Yanagida, "Optical, scintillation and dosimeter properties of MgO transparent ceramic and single crystal," Ceramics International **42**, 5617 (2016).

[7] W. A. Sibley, C. M. Nelson, and Y. Chen, "Luminescence in MgO," J. Chem. Phys. **48**, 4582 (1968).

[8] C. Vaz, C. Moutafis, M. Buzzi, and J. Raabe, "X-ray excited optical luminescence of metal oxide single crystals," Journal of Electron Spectroscopy and Related Phenomena **189**, 1 (2013).

[9] J. Tauc, R. Grigorovici, and A. Vancu, "Optical properties and electronic structure of amorphous germanium," Physica Status Solidi **15**, 627 (1966).

[10] D. M. Roessler and W. C. Walker, "Electronic spectrum and ultraviolet optical properties of crystalline MgO," Phys. Rev. **159**, 733 (1967).

[11] C. Di Valentin and G. Pacchioni, "Spectroscopic properties of doped and defective semiconducting oxides from hybrid density functional calculations," Accounts of chemical research **47**, 3233 (2014).

[12] J. Robertson and S. J. Clark, "Limits to doping in oxides," Phys. Rev. B **83**, 3233 (2011).

[13] S. Radhakrishna and B. Chowdari, "Radiation damage products in ionic crystals impurity doped alkali halides," Fortschritte der Physik **25**, 511 (1977).

[14] E. Vasilchenko, E. Sarmukhanov, and A. Elango, "Electronic excitations localized in NaBr and RbI crystals near vacancy defects of different sizes," physica status solidi (b) **185**, 189 (1994).

[15] D. Attwood, "Soft X-rays and extreme ultraviolet radiation: Principles and applications," Academic press , 63 (1999).

[16] S. Adachi, "Magnesium oxide (MgO). in: Optical constants of crystalline and amorphous semiconductors," Springer, Boston, MA , 412 (1999).

[17] E. D. Palik (editor), "Handbook of optical constants of solids," Academic press **2**, 928 (1998).

[18] A. Miller and D. Finlayson, "Laser sources and applications," CRC Press , 315 (1997).

[19] M. Lai, J. Nicholson, and W. Rudolph, "Multiple pulse operation of a femtosecond Ti:sapphire laser," Optics communications **142**, 45 (1997).

[20] J. Philip, C. D'Amico, G. Cheriaux, A. Couairon, B. Prade, and A. Mysyrowicz, "Amplification of femtosecond laser filaments in Ti:Sapphire," Phys. Rev. Lett. **95**, 163901 (2005).

[21] Y. Guo, S. Lu, L. Su, C. Zhao, H. Zhang, and S. Wen, "Z-scan measurement of the nonlinear refractive index of Nd^{3+}, Y^{3+}-codoped CaF_2 and SrF_2 crystals," Applied Optics **54**, 953 (2015).

[22] D. Golde, T. Meier, and S. W. Koch, "High harmonics generated in semiconductor nanostructures by the coupled dynamics of optical inter- and intraband excitations," Phys. Rev. B **77**, 075330 (2008).

[23] O. Schubert, M. Hohenleutner, F. Langer, B. Urbanek, C. Lange, U. Huttner, D. Golde, T. Meier, M. Kira, S. W. Koch, and R. Huber, "Sub-cycle control of terahertz high-harmonic generation by dynamical bloch oscillations," Nature Photonics **8**, 147 (2014).

[24] T. Meier, G. von Plessen, P. Thomas, and S. W. Koch, "Coherent electric-field effects in semiconductors," Phys. Rev. Lett. **73**, 902 (1994).

[25] G. Vampa, C. R. McDonald, G. Orlando, D. D. Klug, P. B. Corkum, and T. Brabec, "Theoretical analysis of high-harmonic generation in solids," Phys. Rev. Lett. **113**, 073901 (2014).

[26] S. Jiang, H. Wei, J. Chen, C. Yu, R. Lu, and C. D. Lin, "Effect of transition dipole phase on high-order-harmonic generation in solid materials," Phys. Rev. A **96**, 053850 (2017).

[27] J. Li, S. Fu, H. Wang, X. Zhang, B. Ding, B. Hu, and H. Du, "Limitations of the single-active-electron approximation in quantum simulations of solid high-order harmonic generation," Phys. Rev. A **98**, 043409 (2018).

[28] I. Floss, C. Lemell, G. Wachter, V. Smejkal, S. A. Sato, X.-M. Tong, K. Yabana, and J. Burgdörfer, "*Ab initio* multiscale simulation of high-order harmonic generation in solids," Phys. Rev. A **97**, 011401 (2018).

[29] H. Haug and S. Koch, *Theory of transport properties of semiconductor nanostructures* (Springer Science+Business Media Dordrecht, 1998).

[30] M. Wu, S. Ghimire, D. A. Reis, K. J. Schafer, and M. B. Gaarde, "High-harmonic generation from bloch electrons in solids," Phys. Rev. A **91**, 043839 (2015).

[31] X. Liu, X. Zhu, P. Lan, X. Zhang, D. Wang, Q. Zhang, and P. Lu, "Time-dependent population imaging for high-order-harmonic generation in solids," Phys. Rev. A **95**, 063419 (2017).

[32] Y. S. You, D. Reis, and S. Ghimire, "Anisotropic high-harmonic generation in bulk crystals," Nature Physics **13**, 345 (2017).

[33] T. Huang, X. Zhu, L. Li, X. Liu, P. Lan, and P. Lu, "High-order-harmonic generation of a doped semiconductor," Phys. Rev. A **96**, 043425 (2017).

[34] C. Yu, K. K. Hansen, and L. B. Madsen, "Enhanced high-order harmonic generation in donor-doped band-gap materials," Phys. Rev. A **99**, 013435 (2019).

[35] A. Pattanayak, M. M. S., and G. Dixit, "Influence of vacancy defects in solid high-order harmonic generation," Phys. Rev. A **101**, 013404 (2020).

[36] H. Iravani, K. K. Hansen, and L. B. Madsen, "Effects of vacancies on high-order harmonic generation in a linear chain with band gap," Phys. Rev. Research **2**, 013204 (2020).

[37] S. Almalki, A. M. Parks, G. Bart, P. B. Corkum, T. Brabec, and C. R. McDonald, "High harmonic generation tomography of impurities in solids: Conceptual analysis," Phys. Rev. B **98**, 144307 (2018).

[38] C. Kittel, *Quantum Theory of Solids* (Wiley, 1987).

[39] D. Waroquiers, A. Lherbier, A. Miglio, M. Stankovski, S. Poncé, M. J. T. Oliveira, M. Giantomassi, G.-M. Rignanese, and X. Gonze, "Band widths and gaps from the Tran-Blaha functional: Comparison with many-body perturbation theory," Phys. Rev. B **87**, 075121 (2013).

[40] N. Tancogne-Dejean, M. J. Oliveira, X. Andrade, H. Appel, C. H. Borca, G. Le Breton, F. Buchholz, A. Castro, S. Corni, A. A. Correa, *et al.*, "Octopus, a computational framework for exploring light-driven phenomena and quantum dynamics in extended and finite systems," The Journal of Chemical Physics **152**, 124119 (2020).

[41] P. Giannozzi, O. Baseggio, P. Bonfà, D. Brunato, R. Car, I. Carnimeo, C. Cavazzoni, S. de Gironcoli, P. Delugas, F. Ferrari Ruffino, A. Ferretti, N. Marzari, I. Timrov, A. Urru, and S. Baroni, "Quantum espresso toward the exascale," The Journal of Chemical Physics **152**, 154105 (2020), https://doi.org/10.1063/5.0005082.

[42] J. Aramburu, P. García-Fernández, M. Barriuso, and M. Moreno, "Transition metal complexes coupled to vacancies in oxides: Origin of different properties of Cr^{3+} in MgO bounded to a <100> or <110> Mg^{2+} vacancy," The Journal of Physical Chemistry A **117**, 12642 (2013).

[43] M. Novita and K. Ogasawara, "Study on multiplet energies of V^{2+}, Cr^{3+}, and Mn^{4+} in MgO host crystal based on first-principles calculations with consideration of lattice relaxation," Journal of the Physical Society of Japan **83**, 124707 (2014).

[44] J. Czochralski, "Einneues Verfahren zur Messung des Kristallisationsgeschwindigkeit der Metalle," Z. Phys. Chem. **92**, 219 (1918).

[45] D. Fort, "A tri-arc system for growing high-purity crystals of metallic materials," Review of Scientific Instruments **68**, 3504 (1997).

[46] S. C. Rae, "Spectral blueshifting and spatial defocusing of intense laser pulses in dense gases," Optics communications **104**, 330 (1994).

[47] A. Heins, S. C. Singh, and C. Guo, "Electron kinetic energy and plasma emission diagnosis from femtosecond laser produced air plasmas," Physics of Plasmas **24**, 072101 (2017).

[48] V. E. Nefedova, M. F. Ciappina, O. Finke, M. Albrecht, J. Vábek, M. Kozlová, N. Suárez, E. Pisanty, M. Lewenstein, and J. Nejdl, "Determination of the spectral variation origin in high-order harmonic generation in noble gases," Phys. Rev. A **98**, 033414 (2018).

[49] G. Jargot, N. Daher, L. Lavenu, X. Delen, N. Forget, M. Hanna, and P. Georges, "Self-compression in a multipass cell," Opt. Lett. **43**, 5643

(2018).